Chapter 9

# Adsorption, Kinetics and Photoactivity of ZnO-Supported Fly Ash-Sepiolite Ternary Catalyst

Ayşe Neren Ökte

Additional information is available at the end of the chapter

http://dx.doi.org/10.5772/intechopen.70504

**Abstract**

Nanocomposites have been attracting more attention in various fields. In this chapter, ZnO-supported fly ash-sepiolite (ZnO-FA-Sep) was prepared as a ternary composite for the evaluation of adsorption capacities and photocatalytic activities. Characterization studies supplied information about the surface morphology variation before and after ZnO loading within the FA-Sep environment. Strong dark adsorption capacities of the supported catalysts improved their photocatalytic performances, in terms of methyl orange (MO) decolorization and degradation processes. This study not only provided important inspirations for developing support materials but also opened new features to facilitate the photocatalyts' performances.

**Keywords:** supported catalyst, methyl orange, adsorption, kinetics, photocatalysis

## 1. Introduction

Adsorption has been used extensively in industrial processes for separation and purification. Recent research has been focused on the development of low cost adsorbents. Among many alternatives, fly ash cost-effectively improves the performance of products it is added to [1]. Although, significant quantities are being used in a range of applications, it mainly works in tandem with cement in the production of concrete products. However, there is still large amount of fly ash production. An efficient usage of fly ash creates positive environmental impacts. Fly ash use conserves natural resources and avoids landfill disposal of ash products. By making concrete more durable, life cycle costs of roads and structures are reduced. Furthermore, fly ash use partially displaces production of other concrete ingredients, resulting in significant energy savings and reductions in water consumption and greenhouse gas emissions.

Sepiolite is a natural hydrated magnesium silicate fibrous clay with a composition of $Si_{12}Mg_8O_{30}(OH)_4(OH_2)_4{\cdot}8H_2O$. It exhibits high surface area, porosity, good chemical stability and

mechanical behavior [2, 3]. Its applications focused on the use as additives and adsorbents. The crystalline structure is composed of alternating silicate blocks and cavities. The presence of silanol groups (Si-OH) makes use of sepiolite as a support for metals and metal oxide nanoparticles [4].

ZnO is one of the most promising photocatalysts under the ultraviolet radiation to protect the environment by degradation of organic pollutants in water and air. In general, a photocatalytic reaction starts with the generation of electrons and holes by photoexcitation. Then, these charge carriers migrate to the surface of the photocatalyst and react with adsorbed electron acceptors and donors, respectively. Thus, an efficient photocatalyst requires a suitable band-gap, facile separation and transportation of electrons and holes for the feasibility of potential redox reactions. ZnO with its high photo sensitivity and large bandgap plays a significant role for reduction and oxidation processes. However, usage of ZnO nanoparticles in catalytic slurries alone creates fast charge carrier recombination and requires long-time centrifugation for the removal process. An effective way to overcome these difficulties is to immobilize the ZnO nanoparticles on the inner and outer surfaces of inorganic porous supports with the formation of nanocomposite materials [5, 6]. These materials induce high surface area, large pore volume, good dispersion and strong adsorptivity. A synergetic effect is expected in the coexistence of ZnO and a support which eventually transfer species from the support to ZnO or vice versa by the interface created between two phases. Hence, an increase in reaction rates is expected and ZnO/support composites have been postulated as suitable alternative photocatalysts in environmental applications.

The adsorption on the cenospheres and/or plerospheres of fly ashes makes use of them as ideal support materials. Synthesis, characterization, adsorption property and photoactivity of ZnO- or $TiO_2$-loaded fly ash composites are recently examined for anti-corrosion in coatings and also degradation of inorganic and organic pollutants to provide additional way to utilize the waste fly ash [7–13]. Photoactive ZnO nanoparticles supported on sepiolite are also reported for applications in decontamination of pollutants [14–19]. The immobilization of ZnO nanoparticles can be improved within the sepiolite framework due to the net negative charge of the sepiolite. Thus, charge separation efficiency and high adsorption capability can enhance the removal performance for the photodecomposition of organic pollutants.

This chapter is focused on a ternary photocatalyst; ZnO-supported fly ash-sepiolite (ZnO-FA-Sep) by taking advantage from the above-mentioned unique characteristics of fly ash and sepiolite. This composite can be considered as the first approximation of in situ formation of ZnO nanoparticles in presence of a clay (Sep) and an ash material (FA). With this objective, the as-prepared supported catalysts are characterized, structurally examined and evaluated via adsorption ability, kinetics and photocatalytic performance.

## 2. Preparation and characterization of the photocatalysts

ZnO catalysts were synthesized via a co-precipitation route [20]. In a typical preparation step, 0.5 M (or 0.25 or 0.125 M) $Zn(NO_3)_2{\cdot}6H_2O$ was added gradually to 0.5 M (or 0.25 or 0.125 M)

$Na_2CO_3$ solution under vigorous stirring for 2 h at room temperature. The resulting product was collected by centrifugation, washed with deionized water several times, dried at 100°C overnight and calcined at 500°C. Finally, the samples were designated as 0.125 M ZnO, 0.25 M ZnO and 0.5 M ZnO.

Raw Sep and FA used as supports in this study were obtained from Eskişehir-region of Anatolia and Soma (Turkey), respectively. They were characterized by X-ray diffraction and SEM-EDX analyses [18, 19]. Supported catalysts were prepared with the addition of FA-Sep dispersions (1:1 w/w, stirred about 12 h) into the above-mentioned ZnO solutions. The resulting product was collected by centrifugation, washed with deionized water for several times, dried at 100°C overnight and calcined at 500°C. Finally, the catalysts were designated as 0.125 M ZnO-FA-Sep, 0.25 M ZnO-FA-Sep and 0.5 M ZnO-FA-Sep.

X-ray diffraction patterns were recorded on an X-ray diffractometer (Rigaku-D/MAX-Ultima-diffractometer, 40 kV, and 40 mA) equipped with graphite monochromatized Cu-K$\alpha$1 radiation ($\lambda$ = 1.54 Å) at a scan rate of 2° $min^{-1}$. Brunauer-Emmett-Teller (BET)-specific surface area and pores size were determined from the nitrogen adsorption apparatus (Quantachrome Nova 2200e) at 77 K. Prior to the measurements, the samples were pretreated in a vacuum at 473 K for 24 h. The morphology of the products was investigated by scanning electron microscopy (ESEM-FEG/EDAX Philips XL-30) running at an accelerating voltage of 20 kV. The elemental composition of the composites was determined by energy dispersive X-ray spectroscopy (EDS). X-ray photoelectron spectroscopy (XPS) data were recorded with a Thermo Scientific K-Alpha Photoelectron Spectrometer using Al K$\alpha$ (12.5 kV) X-ray source. Calibration of the instrument was done via carbon peak [21, 22]. UV-visible (UV-vis) absorption spectra were recorded with a Shimadzu UV-2450. Diffuse reflectance measurements (DRS) were recorded by using an integrated sphere reflectance accessory with $BaSO_4$ reference.

The photodegradation of methyl orange (MO)-probe molecule in this study was carried out at room temperature in a homemade photocatalytic reactor under UV light (Philips TL 15 W/5BLB, $\lambda$ = 365 nm, an incident photon flux of $4.7 \times 10^{15}$ photons $s^{-1}$) [12, 18]. A typical reaction system included 0.2 g of a catalyst and 200 mL of a known concentration of MO. The suspension was stirred in the dark for 30 min. Thereafter, irradiation was started and UV-vis absorption spectra were recorded to monitor both degradation and decolorization processes. The decrease of the band at 274 nm indicated degradation of MO's aromatic moiety while the one at 464 nm was followed for the decolorization of MO solution. All experiments were performed at room temperature and at pH = 8 (3.27 mg $L^{-1}$ MO in the presence of 0.5 M ZnO-FA-Sep) without concerning the degradation intermediates. Also, measurements were conducted at least twice and the average value was recorded. The degradation and decolorization rate percentages of MO were calculated by the following equation:

$$\text{Degradation (or decolorization)}\% = \frac{C_0 - C}{C_0} \times 100 \quad (1)$$

where $C_0$ was the initial concentration of MO and C was the concentration of MO after "t" minutes irradiation.

## 3. Structural characterization

### 3.1. XRD analysis

XRD patterns of Sep, FA, FA-Sep and the supported catalysts are shown at both low-angle ($2\theta < 10^{\circ}$) and high-angle ($20^{\circ} < 2\theta < 60^{\circ}$) ranges (**Figure 1A**). The characteristic d 1 1 0 reflection of the Sep appears at 7.24° (2$\theta$ ) with a basal spacing of 12.19 Å. The pattern of FA includes amorphous aluminosilicate glass (as major) phase. Quartz ($SiO_2$) reflections of d 1 0 0, d 1 0 1 and d 1 1 0 are detected at 20.8, 26.6 and 36.6° (2$\theta$), respectively. Minor constituents of calcite ($CaCO_3$) reflections of d 1 0 1 and d 1 0 4 are observed at 30° and 48° (2$\theta$), respectively. Lime (CaO) reflection at 62° (2$\theta$ ) of d 104 is also noticed. For the FA-Sep support, the intensities of d 1 1 0 reflection and all other high angle peaks decrease. Supported catalysts reveal d 1 0 0, d 0 0 2, d 1 0 1, d 1 0 2, d 1 1 0, d 1 0 3 and d 2 0 0 crystal planes of ZnO at 31.9, 34.6, 36.4, 47.7, 56.7, 63.1 and 66.6° (2$\theta$), respectively (JCPDS file no. 36-1451). The peak position and basal spacing of the d 1 1 0 reflection do not change significantly for the FA-Sep and supported catalysts due to the non-expandable nature of the Sep. The ZnO signals are intensified with the increasing loading concentrations while the retained FA-Sep peaks decrease significantly.

Scherrer's equation is used to evaluate ZnO crystalline sizes ($D_{ZnO}$) in the supported catalysts. According to the d 1 0 1 reflection of ZnO, $D_{ZnO}$ values are found as 16.1, 13.1, 9.85 and 11.7 nm for 0.25 M ZnO, 0.125 M ZnO-FA-Sep, 0.25 M ZnO-FA-Sep and 0.5 M ZnO-FA-Sep, respectively (**Table 1**). Hence, formation of ZnO aggregates is inhibited in the presence of the FA-Sep support. The reduction in the ZnO crystalline sizes in the form of supported catalysts and the decrements in the FA-Sep reflections may suggest distribution of ZnO nanoparticles over the surface and bulk.

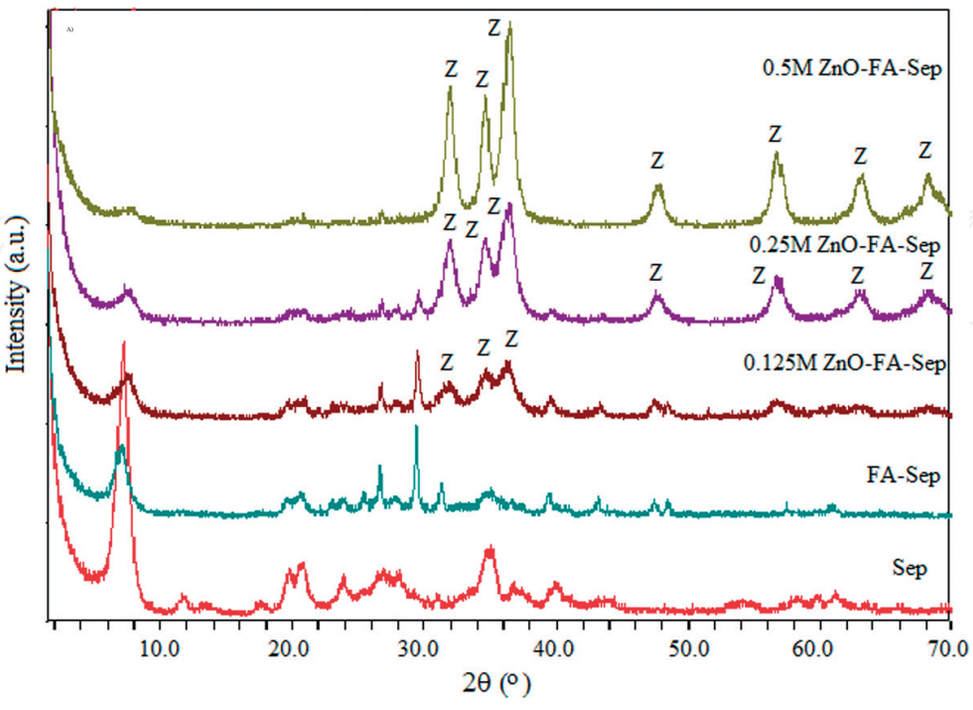


**Figure 1A.** XRD patterns of Sep, FA-Sep and supported catalysts (Z: ZnO).

| Catalysts | $D_{ZnO}$ (nm)[a] | BET ($m^2\ g^{-1}$)[b] | $V_{pore}$ ($cm^3\ g^{-1}$)[c] | $R_{pore}$ (Å)[d] |
|---|---|---|---|---|
| 0.25 M ZnO | 16.08 | 7.58 | 0.012 | 17.7 |
| FA | – | 1.80 | 0.003 | 14.9 |
| Sep | – | 104.5 | 0.140 | 14.9 |
| FA-Sep | – | 46.4 | 0.006 | 15.6 |
| 0.125 M ZnO-FA-Sep | 13.11 | 61.7 | 0.111 | 14.9 |
| 0.25 M ZnO-FA-Sep | 9.85 | 62.3 | 0.121 | 15.4 |
| 0.5 M ZnO-FA-Sep | 11.66 | 50.2 | 0.097 | 14.8 |

[a]Calculated from the (1 0 1) diffraction peak of ZnO using the Scherrer equation.
[b]Determined from nitrogen adsorption–desorption isotherms using BET equation.
[c]Determined from cumulative adsorption pore volume using BJH method.
[d]Determined from adsorption pore size using BJH method.

**Table 1.** Crystalline sizes ($D_{ZnO}$), surface areas (BET), total pore volumes ($V_{pore}$) and pore radius ($R_{pore}$) of 0.25 M ZnO, supports and supported catalysts.

### 3.2. SEM (EDX) analysis

**Figure 1B** shows SEM images of Sep, FA, FA-Sep, 0.25 M ZnO-FA-Sep and elemental mapping images of the supported catalyst. The Sep exhibits a wavy pattern among the layers. The FA displays spherical (with air holes) and non-shaped particles. For the FA-Sep, the structures of the Sep and FA are retained with Si, Ca and Al major, Mg and Fe minor constituents. The

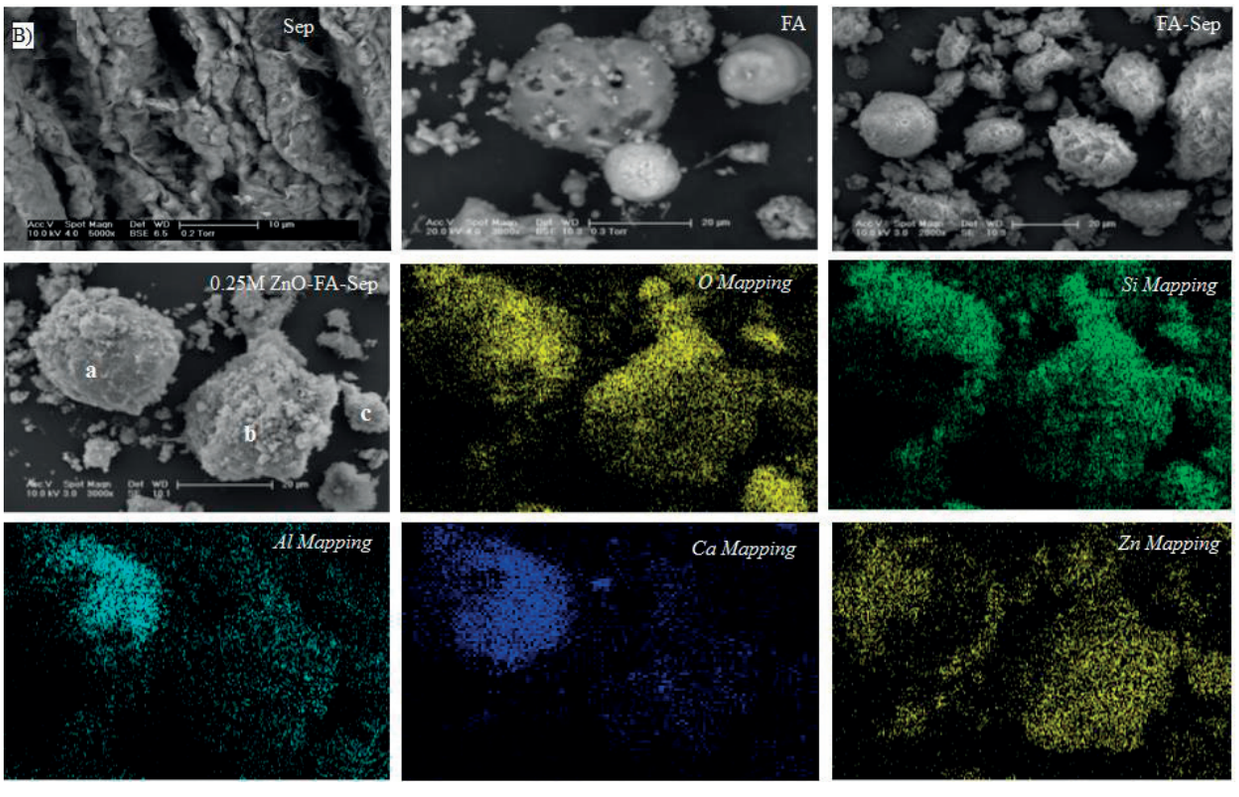


**Figure 1B.** SEM and mapping images of Sep, FA, FA-Sep and 0.25 M ZnO-FA-Sep.

appearance of 0.25 M ZnO-FA-Sep is different from the morphologies of Sep, FA and FA-Sep. The mixed structure of FA spheres and Sep layers suggests hosting of ZnO nanoparticles simultaneously on the spheres and/or non-shaped particles. This is proved by the EDX-spot analysis where Zn percentages are founds as 29 and 69% on the spheres 'a' and 'b' and 66% on the non-shaped particle 'c', respectively. Dominating Zn signals in the mapping images verify the dispersion of ZnO nanoparticles on the FA-Sep support.

### 3.3. Nitrogen adsorption-desorption isotherms

Nitrogen adsorption-desorption isotherms and pore size distributions are shown in **Figure 1C** and **D**, respectively. The non-porous FA and 0.25 M ZnO reveal Type II isotherms. For the Sep,

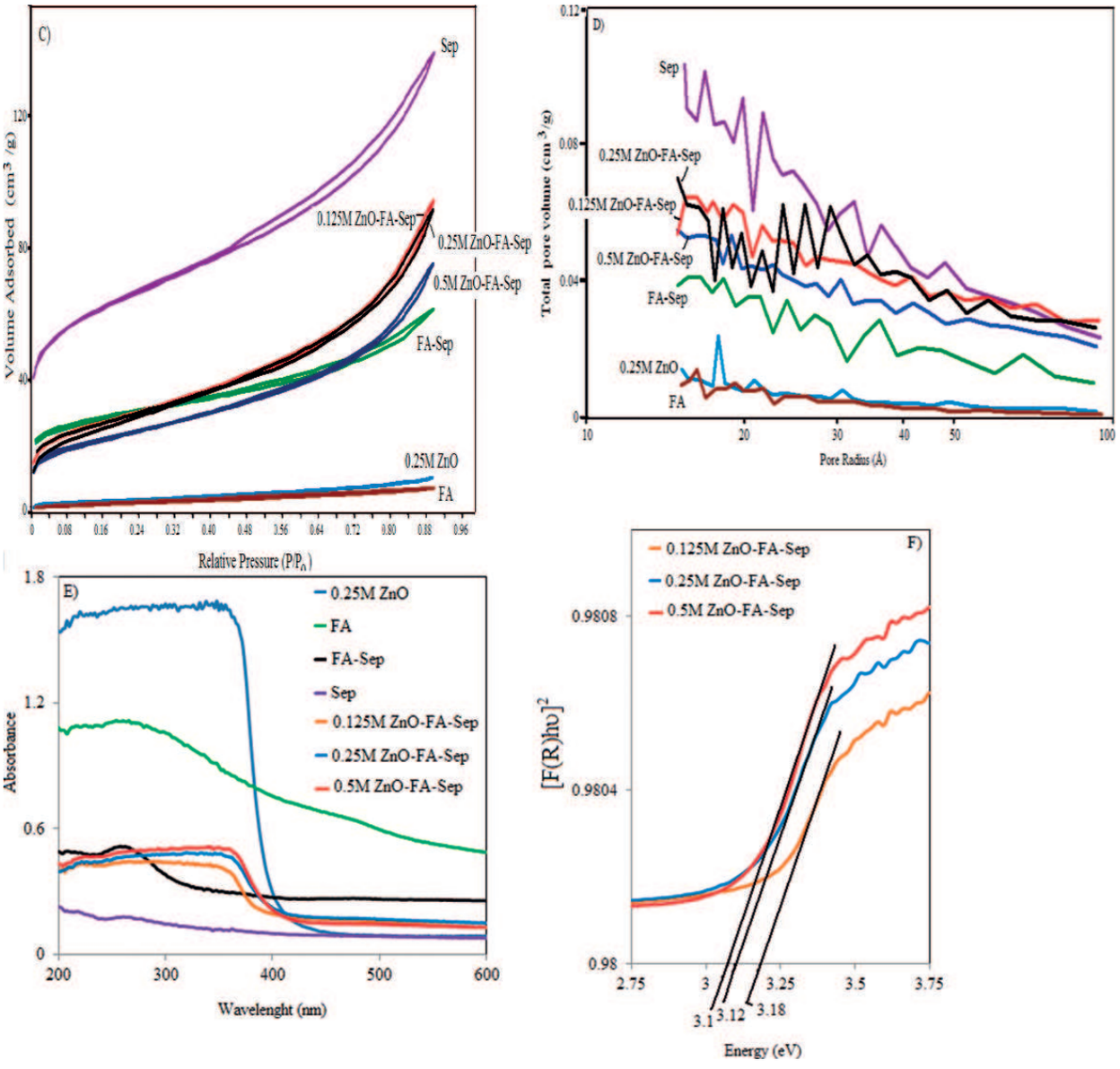


**Figure 1C-F.** (C) nitrogen adsorption/desorption isotherms of Sep, FA, FA-Sep, 0.25 M ZnO, supported catalysts, (D) pores size distribution plots of Sep, FA, FA-Sep, 0.25 M ZnO, supported catalysts, (E) diffuse reflectance spectra of Sep, FA,FA-Sep, 0.25 M ZnO, supported catalysts, (F) Kubelka-Munk transformed reflectance spectra of supported catalysts.

http://dx.doi.org/10.5772/intechopen.70504

FA-Sep and supported catalysts, Type II isotherms are also detected with sites of different affinity to nitrogen and multilayer coverage at high $P/P_0$. Almost similar pore radius is detected for all catalysts and the supports (**Table 1**). The FA-Sep composite and supported catalysts exhibit lower surface areas and pore volumes in comparison to the Sep. This suggests an increment in the number of hosted FA spheres and/or ZnO nanoparticles. In the meantime, supported catalysts possess higher surface areas and pore volumes than the FA-Sep. Thus, enhanced adsorption capacities and degradation abilities are expected in the existence of the supported catalysts.

### 3.4. UV-vis DRS analysis

UV-vis absorption spectroscopies of the FA, Sep, FA-Sep and supported catalysts are presented in **Figure 1E**. Absorption profiles of the supports are similar with extensions in between 200 and 600 nm. 0.25 M ZnO shows its characteristic edge below 400 nm. All supported catalysts reveal this edge with a slight blue shift relative to 0.25 M ZnO and longer wavelength tails are not detected. The band gap energies for 0.125 M ZnO-FA-Sep, 0.25 M ZnO-FA-Sep and 0.5 M ZnO-FA-Sep are evaluated by linear extrapolation and taking the intercept on the *x*-axis as

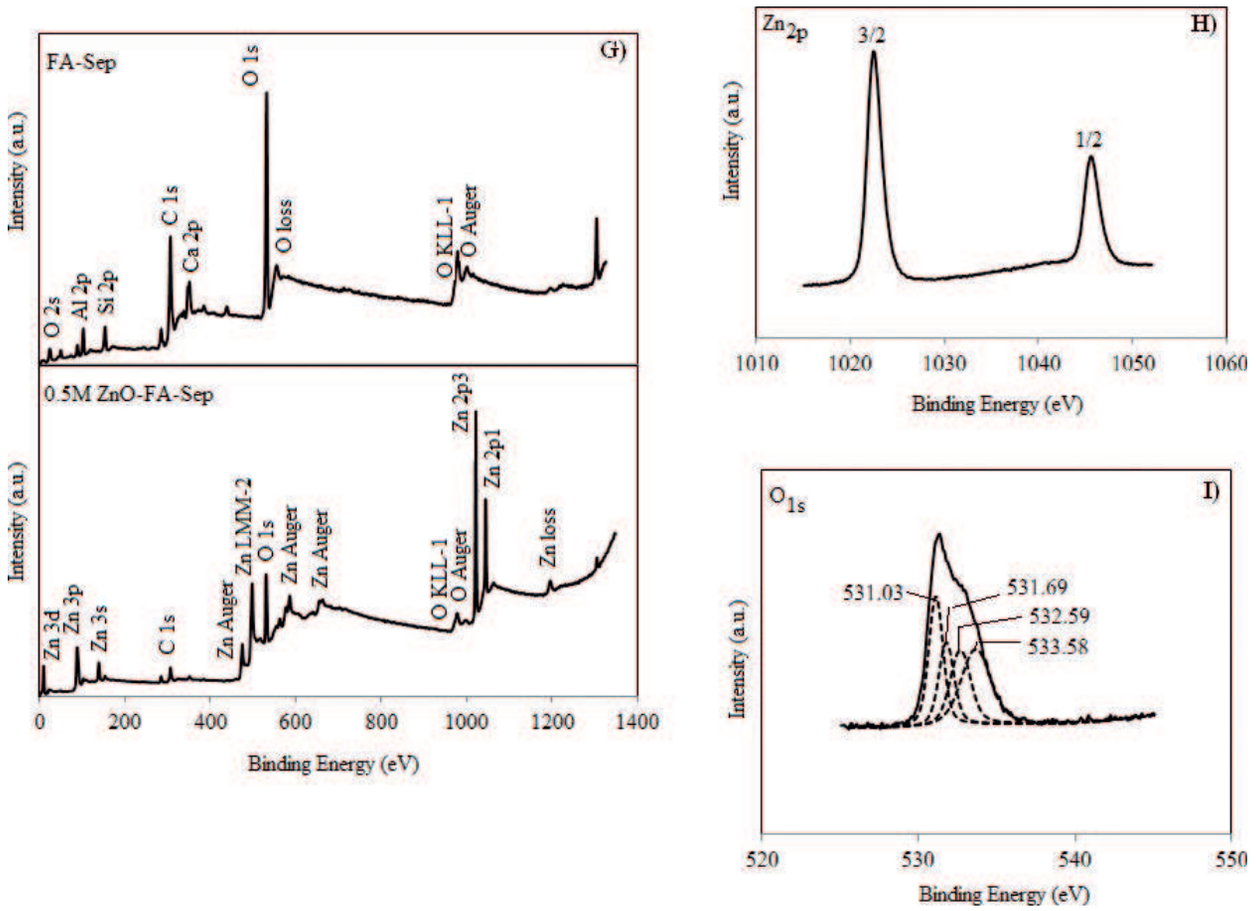


**Figure 1G-I.** (G) XPS survey analysis of FA-Sep and 0.5 M ZnO-FA-Sep, (H) Zn 2p XPS spectra of 0.5 M ZnO-FA-Sep, (I) O 1s XPS spectra of 0.5 M ZnO-FA-Sep.

3.10, 3.12 and 3.18 eV, respectively (**Figure 1F**). Thus, supported catalysts have suitable band gap energies for the degradation of MO under UV-A irradiation.

### 3.5. XPS analysis

XPS analysis is also performed to control the surface structure of the 0.5 M ZnO-FA-Sep. The survey scan reveals Zn peaks in addition to the Al (75.6 eV), Si (103 eV), Ca (347.07 eV), O (531.47 eV) and some Auger peaks of the FA-Sep support (**Figure 1G**). The doublet in Zn peaks corresponds to Zn 2p3/2 and 2p1/2 core levels (**Figure 1H**). Zn exists mainly in the form of $Zn^{2+}$ oxidation state on the catalyst surface owing to the sharpness in Zn 2p3/2 peak [23]. The broad O 1 s signal of the 0.5 M ZnO-FA-Sep catalyst is deconvoluted by four subspectral parts (**Figure 1I**). CaO and $Al_2O_3$ (531.03 eV, 26.9% spectral area), oxygen in the form of $Zn(OH)_2$ (531.69 eV, 18.5% spectral area), $SiO_2$ (532.59 eV, 22.3% spectral area) and adsorbed water (533.58 eV, 32.2% spectral area) are labeled as the components of the supported catalyst.

## 4. Adsorption and photocatalytic applications

### 4.1. Control experiments

Prior to the evaluation of photoactivities of the supported catalysts in detail, two control experiments are designed. As a first step, photolysis of MO is tested under UV illumination and a negligible degradation is found (**Figure 2A**). Then, FA-Sep, 0.25 M ZnO-FA-Sep and 0.5 M ZnO-FA-Sep are examined without irradiation. In the presence of FA-Sep, the remaining MO percentages in the solution are detected as 84% for decolorization and 85% for degradation. However, supported catalysts reveal better adsorption capabilities in comparison to FA-Sep, which further enhanced with the ZnO loading concentration. Accordingly, 0.25 M ZnO-FA-Sep demonstrates 75% (for decolorization) and 73% (for degradation) MO staying in solution within 30 min and thereafter no significant change is noticed. Contrarily, 0.5 M ZnO-FA-Sep shows rapid decrements in both decolorization (7%) and degradation (5.3%) processes within 80 min.

MO exists in the anionic form in water since its natural pH (5.85) is higher than its $pK_a$ (3.4) value [24]. The alkaline character of FA-Sep (pH = 10) solution, hence, induces repulsive forces among the MO molecules and FA-Sep. However, the weak interaction between positively charged species ($Fe_2O_3$, $TiO_2$ as minor phases) within the disordered FA-Sep structure and negatively charged MO moiety induce decrements in MO percentages. The attraction may proceed through the chromophoric (—N═N—) group and declines the absorption band at 464 nm. Simultaneously, weakening in the conjugation disrupts the benzenic rings and decreases the 274 nm band. The presence of ZnO nanoparticles in the supported matrixes is expected to increase the contact among the supported catalysts and MO molecules which eventually facilitate the degradation and decolorization processes.

In the second set, the photoactivities of the supported catalysts are controlled under irradiation (**Figure 2B**). The lowest MO remaining percentages with slower rates are obtained in the presence of 0.125 M ZnO-FA-Sep within 130 min (45% for decolorization and 47% for degradation). The increment in the ZnO concentration improves the performances of the catalysts.

http://dx.doi.org/10.5772/intechopen.70504

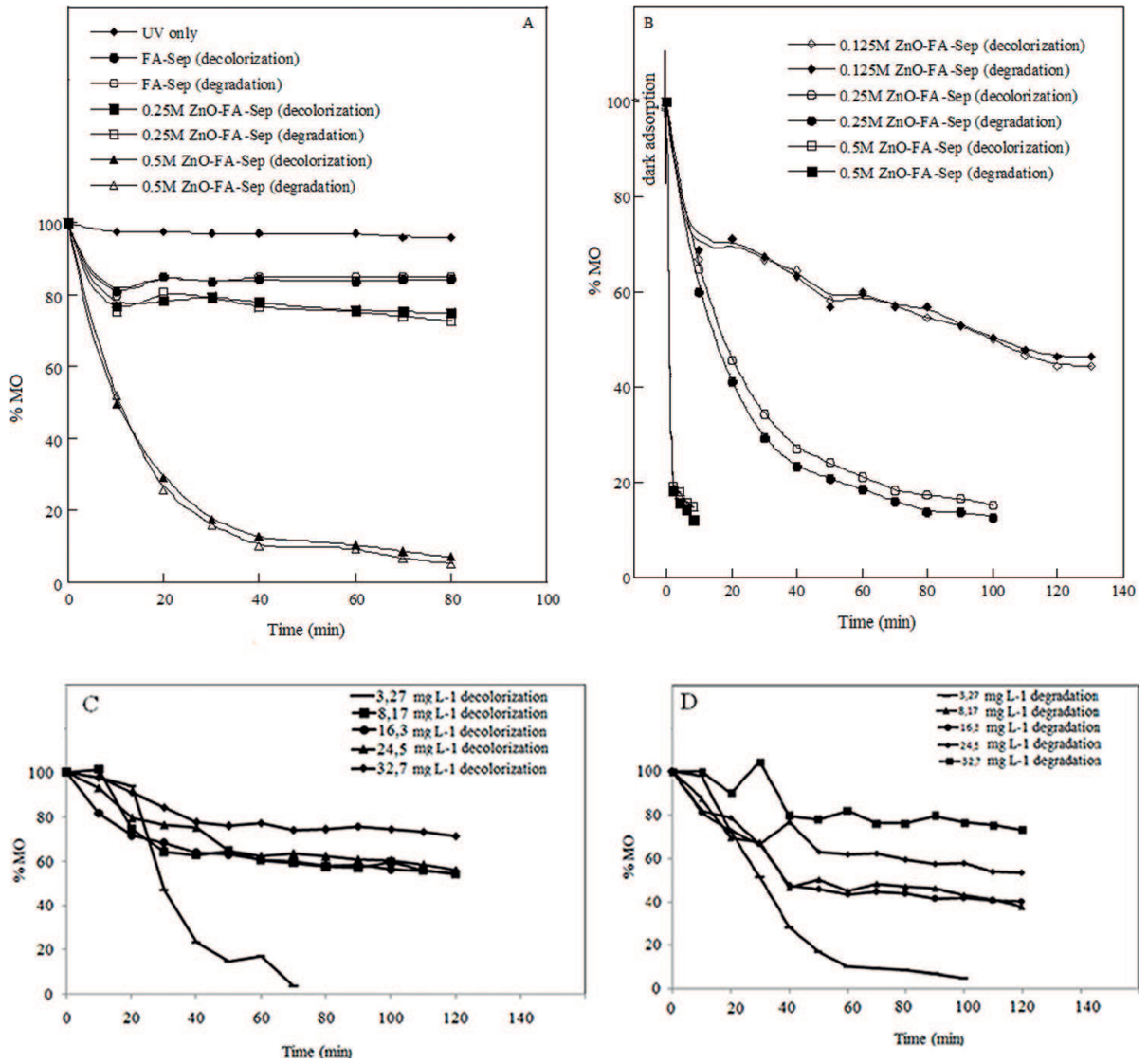


**Figure 2.** (A) Photolysis of MO and dark adsorption experiments of FA-Sep and supported catalysts, (B) photocatalytic activities of the supported catalysts, (C) MO remaining percentages for decolorization and (D) MO remaining percentages for degradation.

0.5 M ZnO-FA-Sep shows the best activity with the lowest MO remaining percentages (15% for decolorization and 12% for degradation) in less than 10 min. Rapid photodegradation of MO is facilitated, due to the synergistic effect of: (1) its adsorption on the mixed structures of FA and Sep, and (2) its photodegradation by the ZnO nanoparticles.

Dark adsorption capacity of 0.5 M ZnO-FA-Sep catalyst is also investigated by varying the initial MO concentrations from 3.27 to 32.7 mg $L^{-1}$ (**Figure 2C** and **D**). It is evident that the amount of adsorbed MO at low initial concentrations is smaller than the corresponding amount at higher initial values, while MO removal percentages decrease significantly with increasing initial MO concentration. The highest MO remaining percentages are noticed with 32.7 mg $L^{-1}$ MO concentration as 73.2 and 71.2% after 120 min for decolorization and degradation processes, respectively. The removal rate of MO is fast up to 30–40 min, and then

gradually decreases with the increase in contact time due to the saturation on the catalyst surface. Contrarily, the lowest MO percentages (around 10% for decolorization and 16% for degradation) are obtained within 60 min for 3.27 mg $L^{-1}$ initial MO concentration. Although surface active sites are more available, very fast adsorption rate and short extraction time are achieved for lower MO concentrations.

### 4.2. Adsorption equilibrium and kinetics

The isotherm analysis of the equilibrium data is examined by fitting the experimental data to Langmuir, Freundlich, Temkin and Dubinin and Radushkevich (D-R) isotherms to find the suitable model [25–31].

*Langmuir isotherm:* Langmuir isotherm assumes that the adsorption takes place at a specific homogeneous site within the adsorbent, all sites are equivalent, and there are no inteactions among the adsorbate molecules. The isotherm can be presented by the following equation [32]:

$$q_e = \frac{K_L a_L C_e}{1 + a_L C_e} \tag{2}$$

where $K_L$ is the adsorption capacity and $a_L$ is the energy of adsorption. Eq. (3) presents the linearized form of Langmuir isotherm. **Figure 3A** supplies data about the $K_L$ (from the *y*-intercept) and $a_L$ (from the slope) values

$$\frac{1}{q_e} = \frac{1}{K_L a_L C_e} + \frac{1}{K_L} \tag{3}$$

The theoretical maximum monolayer adsorption capacity of 0.5 M ZnO-FA-Sep, $q_m$ (mg $g^{-1}$), is also calculated as 48.8 and 28.6 mg $g^{-1}$ from the ratio of $K_L$ to $a_L$ for the decolorization and degradation processes, respectively (**Table 2**).

The separation factor $R_L$ (dimensionless constant) indicates the favorable adsorption within 0–1 range [33] and depending on $a_L$ and $C_0$ values as:

$$R_L = \frac{1}{1 + a_L C_0} \tag{4}$$

The $R_L$ values in the MO concentration range of 3.27–32.7 mg $L^{-1}$ are found to vary in between 0.58–0.12 and 0.51–0.094 for decolorization and degradation, respectively.

The correlation coefficients (0.917 for decolorization and 0.858 for degradation) are reasonable to suggest the applicability of the Langmuir model for the interpretation of the experimental data over the whole concentration range.

*Freundlich isotherm:* Freundlich isotherm predicts heterogeneous adsorption surface and active sites with different energy [34] and presented by the following equation [26] and **Figure 3B**.

$$q_e = K_f C_e^{1/n} \tag{5}$$

http://dx.doi.org/10.5772/intechopen.70504

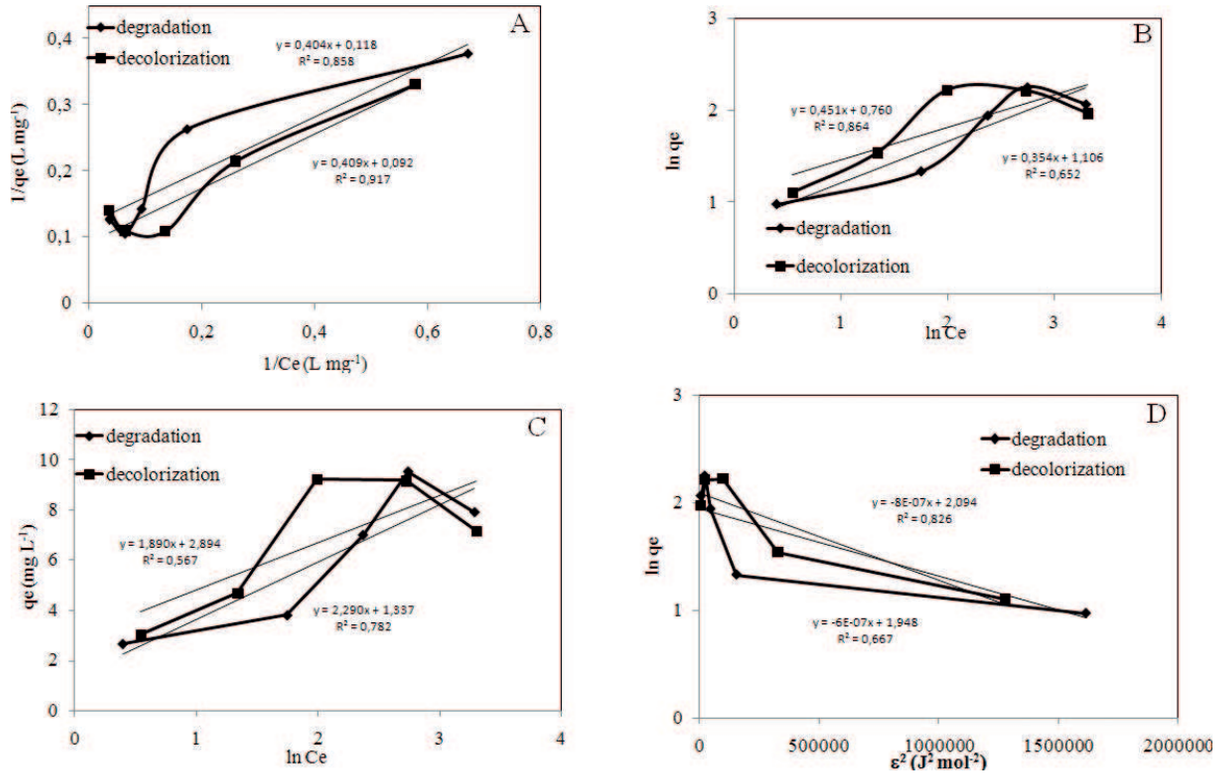


**Figure 3.** (A) Langmuir isotherm, (B) Freundlich isotherm, (C) Temkin isotherm, (D) Dubinin-Radushkevich isotherm.

| | Decolorization | Degradation |
|---|---|---|
| **Langmuir** | | |
| $K_L$ | 10.84 | 8.41 |
| $a_L$ | 0.225 | 0.294 |
| $q_m$ | 48.18 | 28.6 |
| $R^2$ | 0.917 | 0.858 |
| **Freundlich** | | |
| KF | 2.14 | 3.02 |
| 1/n | 0.45 | 0.35 |
| $R^2$ | 0.864 | 0.652 |
| **Temkin** | | |
| $K_T$ | 4.62 | 1.79 |
| $B_T$ | 1.89 | 2.29 |
| $R^2$ | 0.567 | 0.782 |
| **Dubinin-Radushkevich** | | |
| $q_m$ | 8.12 | 1.79 |
| E | 0.79 | 0.91 |
| $R^2$ | 0.826 | 0.667 |

**Table 2.** Adsorption isotherm constants.

where $q_e$ is equilibrium concentration (mg $g^{-1}$), $C_e$ is equilibrium liquid phase concentration (mg $L^{-1}$) and $K_f$ is adsorption capacity. Adsorption intensity is determined by "n". The values of 1/n are found as 0.451 (for decolorization) and 0.354 (for degradation) indicate high tendency of MO for the adsorption onto the supported catalyst. However, Freundlich model is not suitable to describe the relation between sorbed MO molecules and their equilibrium concentrations owing to the lower correlation coefficients (0.864 for decolorization and 0.652 for degradation).

*Temkin isotherm:* The heat of adsorption and the adsorption-binding energy relation are explored by the following Temkin equation [35]:

$$q_e = \frac{RT}{b} \ln (K_{Te} C_e) \tag{6}$$

Eq. (6) can be linearized as

$$q_e = B_T \ln K_T + B_T \ln C_e \tag{7}$$

where $K_{Te}$ is equilibrium binding constant (L $mg^{-1}$), b is the heat of adsorption (J $mol^{-1}$), $B_T$ is related to the heat of adsorption as being equal to RT/b, R is the gas constant and T is the temperature (K). The values of Temkin constants ($K_{Te}$ = 4.62 and $B_T$ = 1.89 for decolorization and $K_{Te}$ = 1.79 and $B_T$ = 2.29 for degradation) and correlation coefficients ($R^2$ = 0.567 for decolorization and $R^2$ = 0.782 for degradation) are found to be lower than the Langmuir values (**Table 2**, **Figure 3C**). Thus, Temkin model does not fit to the corresponding experimental data of MO adsorption on 0.5 M ZnO-FA-Sep.

*Dubinin-Radushkevich (D-R) isotherm:* Dubinin-Radushkevich model is based on heterogeneous surfaces, different sorption sites and steric hindrance effect among adsorbed molecules and bulk species [36]. The linear form of D-R isotherm is expressed by the following equation [31]:

$$\ln q_e = \ln q_m - \beta \varepsilon^2 \tag{8}$$

where $q_e$ is the amount of adsorbate per unit weight of adsorbent (mg $g^{-1}$), $q_m$ is the maximum adsorption capacity (mg $g^{-1}$), β is a coefficient for adsor ption mean free energy ($mol^2\ J^{-2}$) and ε is the Polanyi potential ($\varepsilon = RT \ln(1 + 1/C_e)$).

The $q_m$ values are found using the intercept of the plot as 8.12 and 7.02 mg $g^{-1}$ for decolorization and degradation, respectively (**Table 2**, **Figure 3D**).

The adsorption mean free energy (E; kJ $mol^{-1}$) can be found from the slope as follows

$$E = \frac{1}{\sqrt{-2\beta}} \tag{9}$$

Its value gives information about adsorption mechanism whether it is physical or chemical. If it lies between 8 and 16 kJ $mol^{-1}$, the adsorption process takes place chemically and while E < 8 kJ $mol^{-1}$, the adsorption process proceeds physically [37, 38]. Since adsorption energies

are calculated as 0.79 kJ $mol^{-1}$ for decolorization and 0.91 kJ $mol^{-1}$ for degradation processes, only physical interactions are probable among MO moiety and the supported catalyst. The lower correlation coefficients ($R^2$ = 0.826 for decolorization and $R^2$ = 0.667 for degradation) again represents the poorer fit of the experimental data.

The kinetics of MO adsorption onto 0.5 M ZnO-FA-Sep are studied in terms of pseudo-first order [39], pseudo-second order [40], Elovich [41–43] and intraparticle diffusion [44, 45] models.

*Pseudo-first order model:* Pseudo-first order model describes the adsorption rate based on the adsorption capacity [39].

The differential equation of the model is expressed as follows:

$$\frac{dq_t}{dt} = k_1(q_e - q_t) \tag{10}$$

where $k_1$ is the pseudo-first order rate constant (min), $q_e$ is the adsorption capacity at equilibrium and $q_t$ is the adsorption capacity at time t.

Integrating Eq. (10) for the boundary conditions of $q_t = 0$ at t = 0 and $q_t = q_t$ at t = t gives

$$\ln(q_e - q_t) = \ln q_e - k_1 t \tag{11}$$

Accordingly, the values of $\ln(q_e - q_t)$ are linearly correlated with t by plot of $\ln(q_e - q_t)$ versus t. The rate constant ($k_1$) and $q_e$ can be determined from the slope and intercept of the plot, respectively. The pseudo-first order equation fits well for the first 30 min data and then deviations are noticed. Although rate should be proportional to the first power of MO concentration, the linearity is lost for the higher initial MO concentrations. This may be attributed to the limiting effect of pore diffusion through the adsorption process. For the rapid adsorption of the initial stages, the first order rate constants, $k_1$, decrease with increments in MO concentrations for both decolorization and degradation processes (**Table 3**). It is also noticed that calculated $q_e$ values agree well with the experimental data. The high correlation coefficients show the applicability of pseudo-first order kinetics to the adsorption of MO onto the supported catalyst.

*Pseudo-second-order equation:* The adsorption kinetics may also be described by the pseudo-second order model [40]. The differential equation is given as follows:

$$\frac{dq_t}{dt} = k_2(q_e - q_t)^2 \tag{12}$$

where $k_2$ is the second-order rate constant of adsorption. Integrating Eq. (12) for the boundary conditions of $q_t = 0$ at t = 0 and $q_t = q_t$ at t = t gives

$$\frac{t}{q_t} = \left(\frac{1}{k_2 q_e^2}\right) + \frac{t}{q_e} \tag{13}$$

The linearity obtained in the plot of $t/q_t$ versus t results in $k_2$ value (as the intercept) and $q_e$ value as the equilibrium adsorption capacity (from the slope). Similar to the pseudo-first order kinetics, $k_2$ decreases as the concentration of initial MO increases for both processes (**Table 3**). Although high correlation coefficients are obtained, calculated $q_e$ values are not closer to the experimental values. Moreover, the predicted chemical adsorption cannot be applicable since only physical interactions are suggested between MO molecules and the supported catalyst via D-R model.

*Elovich equation:* The Elovich equation is based on the adsorption capacity and expressed as follows [46–48]:

$$\frac{dq_t}{dt} = \alpha \exp\left(-\beta_{qt}\right) \tag{14}$$

where β is the initial adsorption rate (mg $g^{-1}$ $min^{-1}$) and $\alpha$ is the desorption constant (g $mg^{-1}$). The linearized form of Eq. (14) with boundary conditions of $q_t = 0$ at $t = 0$ and $q_t = q_t$ at $t = t$ is as follows

$$q_t = (1/\beta) \ln(\alpha\,\beta) - (1/\beta) \ln t \tag{15}$$

Elovich parameters are given in **Table 3**. The plot of $q_t$ versus ln t yields a linear relationship with a slope of 1/ β and an intercept of (1/β) ln ($\alpha$ β). The high correlation coefficients indicate suitability of the model for the evaluation of the adsorption process. The limited number of vacant-available sites on the supported catalyst may decrease the possibility of chemical adsorption process through increments in MO concentration. This eventually results in smaller β values in both decolorization and degradation processes. Simultaneously, desorptions from the surface may be enhanced via less strong physical attractions and increase $\alpha$ values.

*Interparticle diffusion model:* The adsorbate species are probably transported from the bulk of the solution into the solid phase through intraparticle diffusion/transport process. The model is expressed by the following equation:

$$q_t = K_{diff} t^{1/2} + C \tag{16}$$

where C (mg $g^{-1}$) is the intercept and $K_{diff}$ is the intraparticle diffusion rate constant (in mg $g^{-1}$ $min^{1/2}$). $K_{diff}$ can be evaluated by the linear correlation of $q_t$ versus $t^{1/2}$ (**Table 3**). As a general trend, $K_{diff}$ values increase with increase of initial MO concentration but for the highest concentrations there seems to be a constancy. This may point out the existence of restricted diffusion for the external mass. Although C values supplies information about the thickness of the boundary layer, experimental data do not exhibit neither an increasing nor a decreasing trend. Thus, the adsorption mechanism cannot be explained by using this model owing to the complex structure of the supported catalyst.

| Models | Parameters | Decolorization | | | | | Degradation | | | | |
|---|---|---|---|---|---|---|---|---|---|---|---|
| | | **3.27 mg $L^{-1}$** | **8.17 mg $L^{-1}$** | **16.3 mg $L^{-1}$** | **24.5 mg $L^{-1}$** | **32.7 mg $L^{-1}$** | **3.27 mg $L^{-1}$** | **8.17 mg $L^{-1}$** | **16.3 mg $L^{-1}$** | **24.5 mg $L^{-1}$** | **32.7 mg $L^{-1}$** |
| First-order kinetic model | $k_1$ | 0.035 | 0.032 | 0.026 | 0.025 | 0.0021 | 0.056 | 0.052 | 0.039 | 0.028 | 0.0039 |
| | $q_e$ | 3.35 | 4.64 | 10.17 | 9.67 | 6.88 | 2.65 | 4.55 | 6.62 | 9.20 | 9.02 |
| | $R^2$ | 0.897 | 0.934 | 0.949 | 0.971 | 0.912 | 0.984 | 0.727 | 0.985 | 0.924 | 0.906 |
| Second-order kinetic model | $k_2$ | $3.83 \times 10^{-3}$ | $1.77 \times 10^{-3}$ | $1.62 \times 10^{-3}$ | $8.36 \times 10^{-4}$ | $7.47 \times 10^{-4}$ | 0.0508 | $7.65 \times 10^{-3}$ | $2.12 \times 10^{-3}$ | $1.38 \times 10^{-3}$ | $1.02 \times 10^{-3}$ |
| | $q_e$ | 6.45 | 6.89 | 16.94 | 16.94 | 9.09 | 5.43 | 4.85 | 9.17 | 16.67 | 13.51 |
| | $R^2$ | 0.697 | 0.941 | 0.846 | 0.856 | 0.852 | 0.916 | 0.987 | 0.998 | 0.903 | 0.898 |
| Elowich | $\alpha$ | 0.158 | 0.383 | 0.464 | 0.510 | 0.560 | 0.273 | 0.526 | 0.651 | 1.095 | 1.256 |
| | $\beta$ | 0.683 | 0.621 | 0.248 | 0.229 | 0.219 | 0.633 | 0.534 | 0.442 | 0.273 | 0.271 |
| | $R^2$ | 0.958 | 0.886 | 0.951 | 0.920 | 0.647 | 0.925 | 0.821 | 0.985 | 0.952 | 0.914 |
| Intraparticle diffusion | $K_{diff}$ | 0.362 | 0.385 | 1.08 | 1.054 | 0.975 | 0.397 | 0.372 | 0.747 | 0.886 | 0.865 |
| | C | 0.12 | 1.45 | 0.29 | 0.76 | 1.67 | 0.153 | 0.931 | 0.978 | 2.14 | 1.513 |
| | $R^2$ | 0.936 | 0.874 | 0.924 | 0.922 | 0.66 | 0.903 | 0.813 | 0.937 | 0.947 | 0.882 |
| Experimental data | $q_e$(exp) | 3.02 | 4.67 | 9.21 | 9.15 | 7.16 | 2.65 | 3.79 | 6.99 | 9.52 | 7.90 |

**Table 3.** Adsorption kinetics constants.


http://dx.doi.org/10.5772/intechopen.70504

### 4.3. Photocatalytic degradation

#### *4.3.1. Kinetics*

The 0.5 M ZnO-FA-Sep is further used to analyze the rate of reactions in the initial concentration range of MO from 3.27 to 24.5 mg $L^{-1}$(**Figure 4A**). The data from the photocatalytic activities is analyzed for the following rate expression

$$\ln \frac{C_0}{C} = kt \tag{17}$$

where $C_0$ is taken as the equilibrium concentration of MO (mg $L^{-1}$) after dark adsorption. The linearity in the plot of $\ln(C_0/C)$ versus t results confirmed the validity of pseudo-first-order kinetics. The rate-constants (k, $min^{-1}$) are calculated from the slopes of the lines.

For the initial concentration of 3.27 mg $L^{-1}$, 88% degradation and 85% decolorization are achieved within 20 min whereas only 44% (degradation) and 43% (decolorization) MO removal are obtained even at 70 min for the concentration of 24.5 mg $L^{-1}$.Similarly, k values decrease from 0.122 to 0.036 $min^{-1}$ (for degradation) and from 0.121 to 0.056 $min^{-1}$ (for decolorization) as the initial concentration of MO increases from 3.27 to 24.5 mg $L^{-1}$(not shown). Since more MO molecules are expected to be adsorbed to the surface of 0.5 M ZnO-FA-Sep as the initial concentration of MO increases, the sorption of both $OH^-$ and $O_2$ will be reduced. Thus, the number of both photogenerated holes and $^{\bullet}OH$ radicals is suppressed and resulted in lower photocatalytic efficiencies. Meanwhile, more photons are absorbed in bulk solutions by the high concentrations of MO. This creates the shortage of photons to activate the supported catalyst.

Additionally, Langmuir-Hinshelwood model is successfully applied to estimate the relationship between the photocatalytic degradation rate and the initial concentration of organic contaminants by the following rearranged form [49, 50].

$$\frac{1}{R} = \frac{1}{kKC_0} + \frac{1}{k} \tag{18}$$

where R is the rate of decolorization (or degradation), K is the adsorption coefficient of MO onto the 0.5 M ZnO-FA-Sep (L $mg^{-1}$), k is the reaction rate constant (mg $L^{-1}$ $min^{-1}$). The linear correlation [0.997 (for degradation) and 0.998 (for decolorization)] in the plot of (1/R) against ($1/C_0$) proved the validity of the model for the as-prepared supported catalysts (**Figure 4B**). Accordingly, both adsorption of MO to 0.5 M ZnO-FA-Sep (K) and photocatalytic degradation of MO by 0.5 M ZnO-FA-Sep (k) are calculated as 0.066 L $mg^{-1}$ and 0.200 mg $L^{-1}$ $min^{-1}$ (for degradation) and 0.177 L $mg^{-1}$ and 0.154 mg $L^{-1}$ $min^{-1}$ (for decolorization).

#### *4.3.2. Comparison with binary composites*

The ternary-supported catalyst (0.5 M ZnO-FA-Sep) is also compared with the binary ones (0.5 M ZnO-Sep and 0.5 M ZnO-FA) and 0.5 M ZnO (**Figure 4C**). After 20 min dark adsorption, supported catalysts show lower MO percentages remaining in the solution than the 0.5 M ZnO (97% for decolorization and 91% for degradation). Meanwhile, 0.5 M ZnO-Sep displays the

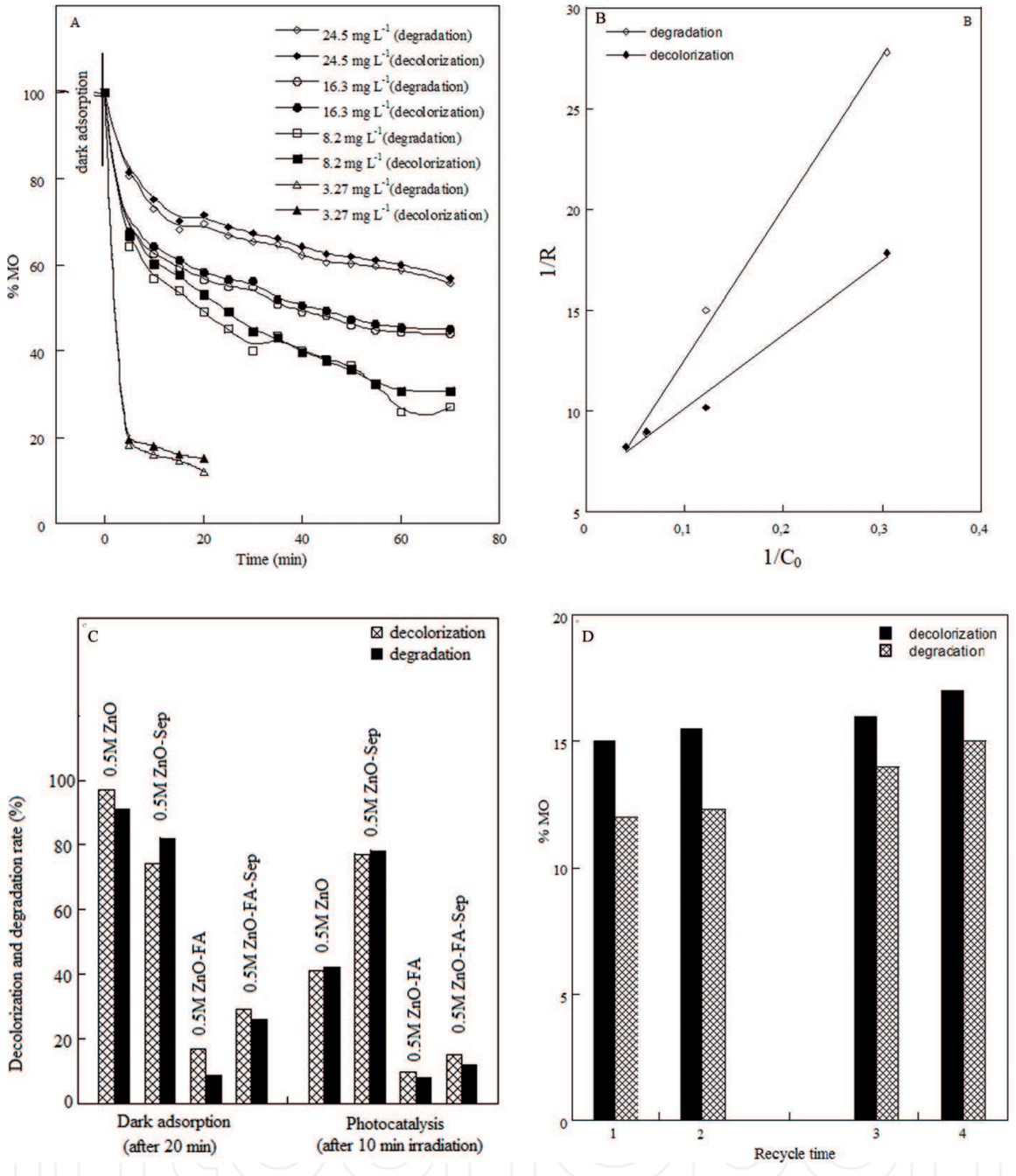


**Figure 4.** (A) Effect of initial MO concentration on the photoactivity of 0.5 M ZnO-FA-Sep, (B) Langmuir-Hinshelwood kinetic analysis in the presence of 0.5 M ZnO-FA-Sep, (C) photoactivity comparison between 0.5 M ZnO-FA-Sep, binary catalysts and 0.5 M ZnO, (D) reuse properties of 0.5 M ZnO-FA-Sep.

highest percentages (74% for decolorization and 82% for degradation) among the binary catalysts. However, the existence of FA spheres within the catalyst matrixes decreases the MO percentages. The lowest values (17% for decolorization and 9% for degradation) are noticed in the presence of 0.5 M ZnO-FA while relatively higher values (29% for decolorization and 26% for degradation) are obtained with 0.5 M ZnO-FA-Sep. Under irradiation, binary catalyst (0.5 M ZnO-Sep) does not work efficiently while the others demonstrate much lower

percentages. Among which, 0.5 M ZnO-FA-Sep competes with the 0.5 M ZnO-FA within 10 min irradiation. The slight difference in the degradation and decolorization percentages may be due the smaller variations in the ZnO crystalline sizes, BET areas and pore volumes ($D_{ZnO}$ = 8.12 nm, BET = 60 $m^2$ $g^{-1}$, $V_{pore}$ = 0.122 $cm^3$ $g^{-1}$ for 0.5 M ZnO-FA and $D_{ZnO}$ = 11.6 nm, BET = 50.2 $m^2$ $g^{-1}$, $V_{pore}$ = 0.097 $cm^3$ $g^{-1}$ for 0.5 M ZnO) [12]. Although FA-Sep has a more complex structure than the FA alone, ZnO nanoparticles in the ternary system are located on the external surfaces of both FA and Sep showing no preference to any of these minerals as detected in the SEM images. Moreover, FA as well as Sep crystals do not agglomerate in the ternary composite owing to their morphological differences in shape and sizes. This creates uniqueness for 0.5 M ZnO-FA-Sep and enhances dispersion of ZnO nanoparticles.

*4.3.3. Reusability*

Furthermore, to investigate the photocatalytic stability of 0.5 M ZnO-FA-Sep, cyclic experiments are carried out under the same experimental conditions (**Figure 4D**). For each run, 0.5 M ZnO-FA-Sep is filtrated, washed and calcined at 500°C for 2 h. After four cycles, the percentage of MO remaining in solution is found to increase only approximately 2% (from 15 to 17% for decolorization process) and 3% (from 12 to 15% for degradation process). The slight increments in the percentages can be attributed to the catalyst loss during each collection and rinsing steps.

## 5. Conclusions

A ternary-supported catalyst has been prepared and characterized by XRD, BET, SEM (EDX), XPS and DRUV techniques. ZnO nanoparticles are found to be dispersed on both FA and Sep minerals. Supported catalysts exhibit higher surface areas and pore volumes than FA-Sep, FA and 0.25 M ZnO·$D_{ZnO}$ sizes do not exhibit significant differences depending on the ZnO loading concentrations. EDX, mapping and XPS analysis evidence the existence of ZnO nanoparticles. Moreover, supported catalysts exhibit an absorption edge similar to 0.25 M ZnO with a slight blue shift. High dark adsorption capacities of the supported catalysts improve their photocatalytic activities, which further enhanced with the ZnO loading concentration. The existence of both FA and Sep with different shapes and sizes decrease their agglomeration and expose more of their surfaces for the adsorption of ZnO nanoparticles.

Future studies will focus on the development of new composites and their applications in environmental issues.

## Acknowledgements

This study was supported by Boğaziçi University Research Foundation (Project No. 17B05P4/13021).

## Author details

Ayşe Neren Ökte

Address all correspondence to: okteayse@boun.edu.tr

Department of Chemistry, Boğaziçi University, Istanbul, Turkey

## References

[1] Yadava KP, Tyagi BS, Singh VN. Effect of temperature on the removal of lead (II) by adsorption on China clay and wollastonite. Journal of Chemical Technology and Biotechnology. 1991;**51**:47-60

[2] Afify AS, Hassan M, Piumetti M, Peter I, Bonelli B, Tulliani JM. Elaboration and characterization of modified sepiolites and their humidity sensing features for environmental monitoring. Applied Clay Science. 2015;**115**:165-173

[3] Ma Y, Zhang GK. Sepiolite nanofiber-supported platinum nanoparticle catalysts toward the catalytic oxidation of formaldehyde at ambient temperature: Efficient and stable performance and mechanism. Chemical Engineering Journal. 2016;**288**:70-78

[4] Li FF, Dai YZ, Gong M, Yu TP, Chen XJ. Synthesis, characterization of magnetic-sepiolite supported with $TiO_2$ and the photocatalytic performance over Cr(VI) and 2,4-dichlorophenol co-existed wastewater. Journal of Alloys and Compounds. 2015;**638**:435-442

[5] Wang B, Zhang GX, Leng X, Sun ZM, Zheng SL. Characterization and improved solar light activity of vanadium doped $TiO_2$/diatomite hybrid catalysts. Journal of Hazardous Materials. 2015;**285**:212-220

[6] Padmanabhan SK, Pal S, Haq EU, Licciulli A. Nanocrystalline $TiO_2$-diatomite composite catalysts: Effect of crystallization on the photocatalytic degradation of rhodamine B. Applied Catalysis A: General. 2014;**485**:157-162

[7] Shi JW, Chen SH, Wang SM, Ye ZL, Wu P, Xu B. Favorable recycling photocatalyst $TiO_2$/CFA: Effects of calcination temperature on the structural property and photocatalytic activity. Journal of Molecular Catalysis A: Chemical. 2010;**330**:41-48

[8] Wang B, Li C, Pang J, Qing X, Zhai J, Li Q. Novel polypyrrole-sensitized hollow $TiO_2$/fly ash cenospheres: Synthesis, characterization, and photocatalytic ability under visible light. Applied Surface Science. 2012;**258**:9989-9996

[9] Visa M, Duta A. Methyl-orange and cadmium simultaneous removal using fly ash and photo-Fenton systems. Journal of Hazardous Materials. 2013;**244–245**:773-779

[10] Visa M, Duca A. $TiO_2$/fly ash novel substrate for simultaneous removal of heavy metals and surfactants. Journal of Chemical Engineering. 2013;**223**:860-868

[11] Yeole K, Kadam P, Mhaske S. Synthesis and characterization of fly ash-zinc oxide nanocomposite. Journal of Materials Research and Technology. 2014;**3**:186-190

[12] Ökte AN, Karamanis D. A novel photoresponsive ZnO-flyash nanocomposite for environmental and energy applications. Applied Catalysis B: Environmental. 2013;**142–143**: 538-552

[13] Ökte AN, Karamanis D, Tuncel D. Dual functionality of $TiO_2$-flyash nanocomposites: Water vapor adsorption and photocatalysis. Catalysis Today. 2014;**230**:205-213

[14] Xu WG, Liu SF, Lu SX, Kang SY, Zhou Y, Zhang HF. Photocatalytic degradation in aqueous solution using quantum-sized ZnO particles supported on sepiolite. Journal of Colloid and Interface Science. 2010;**351**:210-216

[15] Bautista FM, Campelo JM, Luna D, Luque J, Marinas JM. Vanadium oxides supported on $TiO_2$-Sepiolite and Sepiolite: Preparation, structural and acid characterization and catalytic behaviour in selective oxidation of toluene. Applied Catalysis A: General. 2007; **325**:336-344

[16] Arques A, Amat AM, Santos-Juanes L, Vercher RF, Mar´ın ML, Miranda MA. Sepiolites as supporting material for organic sensitisers employed in heterogeneous solar photocatalysis. Journal of Molecular Catalysis A: Chemical. 2007;**271**:221-226

[17] Ökte AN. Advanced Catalytic Materials, Photocatalysis and Other Current Trends. Croatia: INTECH; 2016

[18] Ökte AN, Sayinsöz E. Characterization and photocatalytic activity of $TiO_2$ supported sepiolite catalysts. Separation and Purification Technology. 2008;**62**:535-543

[19] Karamanis D, Ökte AN, Vardoulakis E, Vaimakis T. Water vapor adsorption and photocatalytic pollutant degradation with $TiO_2$-sepiolite nanocomposites. Applied Clay Science. 2011;**53**:181-187

[20] Anandan S, Vinu R, Sheeja Lovely KLP, Gokulakrishnan N, Srinivasu P, Mori T, Murugesan V, Sivamurugan V, Ariga K. Photocatalytic activity of La-doped ZnO for the degradation of monocrotophos in aqueous suspension. Journal of Molecular Catalysis A: Chemical. 2007;**266**:149-157

[21] Lupan O, Chow L, Chai G, Roldan Cuenya B, Naitabdi A, Schulte A, Heinrich H. Nanofabrication and characterization of ZnO nanorod arrays and branched microrods by aqueous solution route and rapid thermal processing. Materials Science and Engineering B. 2007;**145**:57-66

[22] Lupan O, Emelchenko GA, Ursaki VV, Chai G, Redkin AN, Gruzintsev AN, Tiginyanu IM, Chow L, Ono LK, Roldan Cuenya B, Heinrich H, Yakimov EE. Synthesis and characterization of ZnO nanowires for nanosensor applications. Materials Research Bulletin. 2010;**45**:1026-1032

[23] Jing L, Xu Z, Sun X, Shang J, Cai W. The surface properties and photocatalytic activities of ZnO ultrafine particles. Applied Surface Science. 2011;**180**:308-314

[24] Guo P, Wang X, Guo H. $TiO_2$/Na-HZSM-5 nano-composite photocatalyst: Reversible adsorption by acid sites promotes photocatalytic decomposition of methyl orange. Applied Catalysis B: Environmental. 2009;**90**:677-687

[25] Langmuir I. The constitution and fundamental properties of solids and liquids. Part I. Solids. Journal of the American Chemical Society. 1916;**38**:2221-2295

[26] Freundlich HMF. Over the adsorption in solution. The Journal of Physical Chemistry. 1906;**57**:385-470

[27] Ghaedi M, Khajesharifi H, Hemmati Yadkuri A, Roosta M, Sahraei R, Daneshfar A. Cadmium hydroxide nanowire loaded on activated carbon as efficient adsorbent for removal of Bromocresol Green. Spectrochimica Acta Part A. 2012;**86**:62-68

[28] Zhang H, Tang Y, Liu X, Ke Z, Su X, Cai D, Wang X, Liu Y, Huang Q, Yu Z. Improved adsorptive capacity of pine wood decayed by fungi Poria cocos for removal of malachite green from aqueous solutions. Desalination. 2011;**274**:97-104

[29] Temkin MJ, Pyzhev V. Recent modifications to Langmuir isotherms. Acta Physiochimica URSS. 1940;**12**:217-222

[30] Uluozlu OD, Sari A, Tuzen M, Soylak M. Biosorption of Pb (II) and Cr (III) from aqueous solution by lichen (*Parmelina tiliaceae*) biomass. Bioresource Technology. 2008;**99**:2972-2980

[31] Sari A, Tuzen M. Kinetic and equilibrium studies of biosorption of Pb(II) and Cd(II) from aqueous solution by macrofungus (*Amanita rubescens*) biomass. Journal of Hazardous Materials. 2009;**164**:1004-1011

[32] Langmuir I. The adsorption of gases on plane surfaces of glass, mica and platinum. Journal of the American Chemical Society. 1918;**40**:1361-1403

[33] McKay G, Blair HS, Garden JR. Adsorption of dyes on chitin. 1. Equilibrium studies. Journal of Applied Polymer Science. 1982;**27**:3043-3057

[34] Gunay A, Arslankaya E, Tosun I. Lead removal from aqueous solution by natural and pretreated clinoptilolite: Adsorption equilibrium and kinetics. Journal of Hazardous Materials. 2007;**146**:362-337

[35] Temkin MJ, Pyzhev V. Recent modifications to Langmuir isotherms. Acta Physiochimica URSS. 1940;**12**:217-222

[36] Deliyanni EA, Nalbandian L, Matis KA. Adsorptive removal of arsenites by a nanocrystalline hybrid surfactant–akaganeite sorbent. Journal of Colloid and Interface Science. 2006;**302**:458-466

[37] Dubinin MM, Radushkevich LV. Equation of the characteristic curve of activated charcoal. Chemisches Zentralblatt. 1947;**1**:875

[38] Dubinin MM. The potential theory of adsorption of gases and vapors for adsorbents with energetically non-uniform surface. Chemical Reviews. 1960;**60**:235-266

[39] Dubinin MM. Modern state of the theory of volume filling of micropore adsorbents during adsorption of gases and steams on carbon adsorbents. Zhurnal Fizicheskoi Khimii. 1965;**39**:1305-1317

[40] Radushkevich LV. Potential theory of sorption and structure of carbons. Zhurnal Fizicheskoi Khimii. 1949;**23**:1410-1420

[41] Kundu S, Gupta AK. Investigation on the adsorption efficiency of iron oxide coated cement (IOCC) towards As(V)—kinetics, equilibrium and thermodynamic studies. Colloids and Surfaces A: Physicochemical and Engineering Aspects. 2006;**273**:121-128

[42] Lagergren S. Zur theorie der sogenannten adsorption geloster stoffe kungligasvenska vetenskapsakademiens. Handlingar. 1898;**24**:1-39

[43] Ho YS, McKay G, Wase DAJ, Foster CF. Study of the sorption of divalent metal ions on to peat. Adsorption Science & Technology. 2000;**18**:639-650

[44] Chien SH, Clayton WR. Application of Elovich equation to the kinetics of phosphate release and sorption on soils. Soil Science Society of America Journal. 1980;**44**:265-268

[45] Sparks DL. Kinetics of Reaction in Pure and Mixed Systems in Soil Physical Chemistry. Boca Raton: CRC Press; 1986

[46] Chang Y, Lye ML, Zeng HC. Large-scale synthesis of high-quality ultralong copper nanowires. Langmuir. 2005;**21**:3746-3748

[47] Sahraei R, Motedayen Aval G, Goudarzi A. Compositional, structural, and optical study of nanocrystalline ZnS thin films prepared by a new chemical bath deposition route. Journal of Alloys and Compounds. 2008;**466**:488-492

[48] Ghaedi M, Ansari A, Habibi MH, Asghari AR. Removal of malachite green from aqueous solution by zinc oxide nanoparticle loaded on activated carbon: Kinetics and isotherm study. Journal of Industrial and Engineering Chemistry. 2014;**20**:17-28

[49] Yang L, Yu LE, Ray MB. Degradation of paracetamol in aqueous solutions by $TiO_2$ photocatalysis. Water Research. 2008;**42**:3480-3488

[50] Yang H, Li G, An T, Gao Y, Fu J. Photocatalytic degradation kinetics and mechanism of environmental pharmaceuticals in aqueous suspension of $TiO_2$: A case of sulfa drugs. Catalysis Today. 2010;**153**:200-207